


## Original article

# Correlations of residual oil distribution with pore structure during the water flooding process in sandstone reservoirs

Qi Zhang<sup>1,2</sup>, Yongfei Yang<sup>1,2</sup>, Dingyuan Wang<sup>1,2</sup>, Hai Sun<sup>1,2</sup>, Junjie Zhong<sup>1,2</sup>, Jun Yao<sup>1,2</sup>, Vadim Lisitsa<sup>3</sup>

<sup>1</sup>Research Center of Multiphase Flow in Porous Media, School of Petroleum Engineering, China University of Petroleum (East China), Qingdao 266580, P. R. China

<sup>2</sup>National Key Laboratory of Deep Oil and Gas, China University of Petroleum (East China), Qingdao 266580, P. R. China

<sup>3</sup>Institute of Petroleum Geology and Geophysics SB RAS, 3 Koptug ave., Novosibirsk 630090, Russia

### Keywords:

Porous media  
direct numerical simulation  
imbibition  
pore structure  
residual oil

### Cited as:

Zhang, Q., Yang, Y., Wang, D., Sun, H., Zhong, J., Yao, J., Lisitsa, V. Correlations of residual oil distribution with pore structure during the water flooding process in sandstone reservoirs. *Advances in Geo-Energy Research*, 2024, 12(2): 113-126.

<https://doi.org/10.46690/ager.2024.05.04>

### Abstract:

The displacement of residual oil by water flooding in porous media is an important mechanism of enhanced oil recovery in many sandstone reservoirs. Nonetheless, our basic understanding of the influence of complex pore geometries of natural porous media on fluid distribution is still incomplete. Herein, two-phase flow simulations were performed to investigate the pore-scale dynamics of imbibition in a heterogeneous sandstone rock sample. Furthermore, the relationship between residual oil distribution and pore structure parameters was quantitatively characterized based on a pore-throat segmentation method. The findings suggest that the pore-scale displacement and snap-off processes have a strong dependence on the coordination number and aspect ratio. The entrapment and remobilization of oil clusters were also analyzed under continuous and discontinuous displacement modes. In addition, a new quantitative method to evaluate the displacement potential and mobilization pattern of remaining oil was presented and discussed. Statistical analysis revealed that the development of sub-pathways and the suppression of snap-off are responsible for the decrease in residual oil saturation with increasing capillary number during water injection. Moreover, the connected residual oil clusters trapped in pores with high coordination number prefer to be displaced and produced. Finally, the displacement modes with different capillary numbers under different initial oil distributions were evaluated to explain the effect of pore structure. By incorporating these correlations of displacement events with pore-throat geometry, existing predictive models can be improved, which could be helpful for the fine tapping of highly disconnected remaining oil in sandstone reservoirs.

## 1. Introduction

Two-phase flow through geological porous media occurs during the production of oil and gas development. The macro-scale efficiency of oil recovery processes comprehensively reflects the micro-structure of reservoir rock and the dynamics of pore-scale events such as snap-off (Blunt et al., 2013; Zhang et al., 2022; Wang et al., 2023a). Especially, the pore structure characteristics of reservoir rocks are among the key factors controlling the trapping and mobilization of oil during water flooding displacement. The general consensus is that

the heterogeneity of pore morphology controls the type and evolution of pore-scale events that occur during imbibition processes and hence governs the final residual oil distribution (Zacharoudiou et al., 2017; Pak et al., 2023). To further enhance the oil recovery of oilfields at the high water cut stage, it is necessary to extend the pore-scale physical understanding of the relationship between dynamic flow behavior and pore geometry (Li et al., 2018).

Experiments using micro-scale models have been carried out for many years to uncover the foundations of fluid dis-

placement processes at the pore scale. Three-dimensional images of fluid distribution in rocks under different conditions of pressure, temperature and displacement mode, representative of oil reservoirs, were generated to explore the residual oil trapped mechanisms (Yang et al., 2013; Andrew et al., 2014; Pak et al., 2015; Zhang et al., 2023). Changes in the distribution of residual oil in rocks with different pore structure types can be quantified using X-ray microtomography (Wang et al., 2019; Yang et al., 2019, 2020). Mohamed et al. (2020) conducted micro-scale core-flooding experiments to examine how the sequence of flow processes impacts the pore scale displacement mechanisms. Andersson et al. (2018) quantitatively characterized the influence of geometric pore structure on the mobility or immobilization of fluids. A strong correlation between residual oil saturation and pore morphology has been reported (Kimbrel et al., 2022; Gong et al., 2024). However, the main limitation of this method is that the dynamics of two-phase flow are not taken into consideration, as it is based on static or quasi-static experimental data. With new advancements in high-resolution imaging techniques, it has become possible to visualize the dynamics of multiple fluids in the pore space and quantify it using time resolved four dimensions X-ray imaging. This provides important insights into various displacement events such as pore-filling, snap-off and trapping during drainage and imbibition processes (Singh et al., 2017; Gao et al., 2021). Moreover, this type of experiment can also serve as a basis to validate the flow simulation results. Mascini et al. (2021) investigated multiphase flow in sandstones with different wetting properties to visualize and explore the complex interplay between mixed wettability and pore structure. Singh et al. (2022) conducted a time-resolved tomographic drainage-imbibition experiment on a carbonate rock sample, and provided correlations for displacement events as a function of pore-throat geometry through pore-by-pore analysis. By combining experimental data with a pore network model, a work flow has been presented to investigate the relationships between pore structure and dynamic pore filling events (Ellman et al., 2024). It should also be noted that effect of pore structure is indistinguishable from that of local wettability or other factors, while the local flow conditions of a porous sample are hard to keep constant during the experimental process.

A number of computational studies have been performed to investigate the impact of two-phase flow dynamics characterized by pore structure and capillary number on residual oil distribution (Qin et al., 2023; Wang et al., 2023c). These provide the opportunity for a detailed investigation of this problem by altering the parameters over a wider range by simulation, not easily achieved through experiments. Pore-network models comprise a widely used numerical method for studying pore filling events controlled by capillary pressure as a function of pore geometry (Nguyen et al., 2006; Joekar-Niasar et al., 2010; Bultreys et al., 2020). However, the flow formulas considered by pore-network models are based on the quasi-static criterion, and thus dynamic factors are ignored in these formulas. To examine the flow behavior in porous media, direct two-phase flow simulation has also been carried out (Wang et al., 2023b). Shams et al. (2018) studied the effect of geometry and flow

rate on the formation of disconnected ganglia through simple pore geometries. They clarified the blob mobilization mechanism during imbibition; however, these studies only considered simple geometries. Recently, different types of complex geological porous media were used to predict oil trapping and residual saturation (Pereira, 2019; Patel et al., 2019; Michels et al., 2021). The residual oil distribution and flow behavior under various wetting conditions were simulated, and their results revealed two circulating modes in the pore corners of the remaining oil ganglia during water flooding (Guo et al., 2019; Yang et al., 2021). Aziz et al. (2020) evaluated the impact of wettability change on two-phase flow dynamics in two synthetic pore geometries during low-salinity water flooding. According to their simulation data, the ability of remobilization of the trapped oil would be affected by the variation in pore radius distribution. Furthermore, most studies have focused on describing the effects of displacement scenarios (e.g., capillary numbers) and wettability on oil saturation and the resulting fluid distributions, while the relationship of fluid occupancy and mobilization mechanism with heterogeneous pore-throat geometry during the high water cut stage have received relatively little attention.

As illustrated above, the relationship between fluid occupancy and pore structure parameters remains undefined, hence it is the focus of this paper. Immiscible two-phase flow simulations were used to investigate the effect of pore structure on the pore-scale dynamics of imbibition in a heterogeneous sandstone sample. This paper is organized as follows. First, the direct numerical simulation method and the validation using pore-doublet models are presented. Then, three kinds of pores are defined to characterize the residual oil distribution pattern. Novel correlations of residual oil distribution with pore-throat geometry are described, which shows a strong dependence of pore-scale displacement processes on the coordination number, pore shape factor and aspect ratio. The mobilization of oil clusters is further analyzed under continuous and discontinuous displacement modes. Finally, it is evaluated whether and how the pore geometry and capillary number can promote the transformation of phase interface, leading to the entrapment and remobilization of oil ganglia in the non-wetting phase.

## 2. Methods

### 2.1 Two-phase flow modeling

Two-phase flow numerical simulation at the pore-scale is conducted, where the effect of capillary forces can be explicitly described based on a finite volume discretization of the Navier-Stokes equations. The mathematical formulations are based on a single-fluid continuum approach, thus single-field equations are used for continuity and momentum. The mass and momentum conservation equations for isothermal, incompressible, Newtonian fluids are as follows:

$$\nabla \cdot \mathbf{u} = 0 \quad (1)$$

$$\frac{D}{Dt}(\rho \mathbf{u}) - \nabla \cdot [\mu(\nabla \mathbf{u} + (\nabla \mathbf{u})^T)] = -\nabla p + \mathbf{f} \quad (2)$$

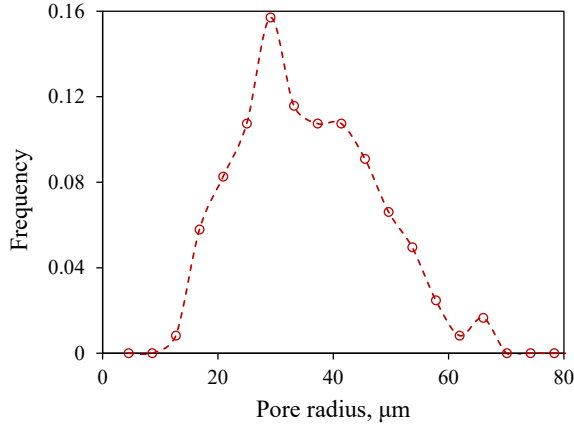


**Fig. 1.** Pore radius distribution curve of the sandstone sample.

where  $\mathbf{u}$  represents the velocity vector and  $p$  represents the pressure;  $t$  represents the time;  $\rho$  and  $\mu$  are respectively fluid density and viscosity;  $\mathbf{f} = \rho\mathbf{g} + \mathbf{f}_c$  represents all external forces,  $\rho\mathbf{g}$  is the gravity force that is ignored in our simulation;  $\mathbf{f}_c$  characterizes the contribution of capillary force to fluid momentum caused by the fluid-fluid interfacial tension  $\sigma$ .

The volume-of-fluid method is employed to track the location of phase interface using an indicator function. In this method,  $\alpha$  represents volume fractions of one of the two fluids in each grid cell. If the cell is completely saturated with a fluid, then  $\alpha = 1$  or  $\alpha = 0$ . At the interface, the value of  $\alpha$  varies smoothly between 0 and 1. This is evolved using the following advection equation:

$$\frac{\partial \alpha}{\partial t} + \nabla \cdot (\alpha \mathbf{u}) = 0 \quad (3)$$

Combined with indicator function  $\alpha$ , the fluid density  $\rho$  and viscosity  $\mu$  denote single field variables, which can be defined as:

$$\rho = \alpha \rho_o - (1 - \alpha) \rho_w \quad (4)$$

$$\mu = \alpha \mu_o - (1 - \alpha) \mu_w \quad (5)$$

where  $\rho_o$  and  $\rho_w$  represent the fluid density of oil and water,  $\mu_o$  and  $\mu_w$  represent the viscosity of oil and water.

Assuming that the interfacial tension  $\sigma$  is constant, capillary term  $\mathbf{f}_c$  can be obtained as a volumetric force:

$$\mathbf{f}_c = \sigma \kappa \mathbf{n} \delta \quad (6)$$

where  $\kappa = \nabla \cdot \mathbf{n}$  represents the local interface curvature;  $\mathbf{n} = \nabla \alpha / |\nabla \alpha|$  is the local unit vector normal to the interface, which can be calculated using the gradient of an indicator function;  $\delta$  represents a delta function located on the interface, which is non-zero only at the interface points. Wetting effects are also considered by modifying  $\mathbf{n}$  in accordance with a prescribed contact angle  $\theta$  in the boundary regions where the phase interface joins a solid wall.

The capillary force can be achieved by the Continuum-Surface-Force (CSF) method (Brackbill et al., 1992). However, prior research has demonstrated that the CSF model induces nonphysical spurious currents, resulting in numerical inaccuracies in the calculation of the surface tension force for small

capillary numbers ( $Ca < 0.01$ ) (Ubbink and Issa, 1999). To limit the effect of spurious currents, an interface compression term  $-\nabla \cdot (\alpha(1 - \alpha)\mathbf{u}_r)$  is introduced to sharpen the interface and increase interface resolution (Rusche, 2002):

$$\frac{\partial \alpha}{\partial t} + \nabla \cdot (\alpha \mathbf{u}) - \nabla \cdot (\alpha(1 - \alpha)\mathbf{u}_r) = 0 \quad (7)$$

where  $\mathbf{u}_r$  represents the relative velocity between the two phases. This additional term is included only in the interface region due to the term  $\alpha(1 - \alpha)$ , so it does not affect other solution regions (Gravelle et al., 2017).

Raeini et al. (2012) developed a sharp surface force (SSF) model for the calculation of curvature and Dirac delta function. By interpolating the value of indicator function from the faces of grid cells to their centers, and doing an inverse calculation, the smoothed indicator function  $\alpha_s$  can be obtained (Raeini et al., 2012):

$$\alpha_s = C_{sk} \langle \langle \alpha \rangle_{c \rightarrow f} \rangle_{f \rightarrow c} + (1 - C_{sk}) \alpha \quad (8)$$

where coefficient  $C_{sk}$  should be less than one to ensure computational stability.

Finally, the calculation for smoothed surface tension  $F_{SSF}$  is expressed as (Raeini et al., 2012):

$$F_{SSF} = -\sigma \nabla \cdot \left( \frac{\nabla \alpha_s}{|\nabla \alpha_s|} \right) \nabla \alpha_{sh} \quad (9)$$

where  $\alpha_{sh}$  denotes a sharpened indicator function, defined by (Raeini et al., 2012):

$$\alpha_{sh} = \frac{1}{1 - C_{sh}} \left[ \min \left( \max \left( \alpha, \frac{C_{sh}}{2} \right), 1 - \frac{C_{sh}}{2} \right) - \frac{C_{sh}}{2} \right] \quad (10)$$

where  $C_{sh}$  represents a sharpening coefficient. If  $C_{sh} = 0$ , then  $\alpha_{sh}$  is equal to  $\alpha$  (the original CSF formulation); if  $C_{sh} = 1$ , then a sharper implementation of the capillary forces will be achieved. In terms of improving numerical stability and robustness at the interfaces,  $C_{sk}$ ,  $C_{sh}$  are equal to 0.5 in our simulations. More details of this method can be found in previous work (Raeini et al., 2012; Shams et al., 2018).

## 2.2 Simulation conditions

In order to examine the dynamics of residual oil under reservoir circumstances, a flow simulation model was applied for the pore space of a three-dimensional heterogeneous sandstone sample. The computational pore geometry was 1.59 mm  $\times$  0.795 mm  $\times$  0.795 mm, and the porosity  $\Phi$  of the model is 0.166. Based on the reconstructed CT images, other pore structure parameters (i.e., pore and throat radius, pore shape factor, coordination number, and average aspect ratio) describing the pores and throats were obtained using a pore-throat segmentation approach (Raeini et al., 2017). This method segments pores by applying a watershed algorithm to the Euler distance map of isolated pore space, and identifies throats as boundary surfaces at the narrowest region of the neighboring pores. The quantitative topological structure parameters and permeability can be extracted by the pore network model. The detailed parameters are shown in Table 1 and Fig. 1. The unstructured mesh was created using SnappyHexMesh. The total number of computational grid cells after meshing was

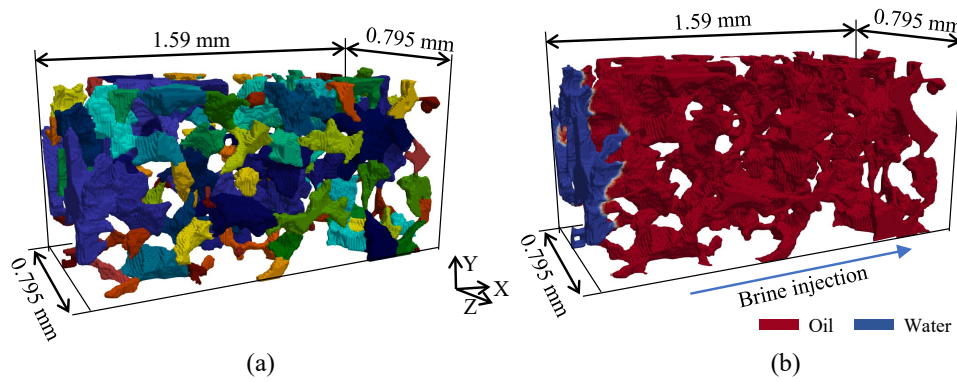


**Fig. 2.** (a) Visualization of the labeled mesh of pore space for the sandstone sample (different colors represent different pore elements) and (b) initial condition for the indicator function.

**Table 1.** Pore structure parameters of the sandstone sample.

Items	Value
Permeability ( $10^{-3} \mu\text{m}^2$ )	1,695.75
Pore number (-)	121
Throat number (-)	189
Average pore radius ( $\mu\text{m}$ )	33.5
Average throat radius ( $\mu\text{m}$ )	27.4
Average coordination number (-)	3.08
Average aspect ratio (-)	1.95

332,356 (the mesh sensitivity analysis was performed in previous work (Yang et al., 2023)). The labels of each pore element were also converted into the mesh constrained by the location of the center of grid. The labeled pore model is shown in Fig. 2(a), where the different color represents different pore elements. The labeled simulation model could provide more reference for describing the fluid flow behavior.

The two-phase flow simulations were performed by implementing the governing equations in the typical volume-of-fluid-based interFoam solver in OpenFOAM (Weller et al., 1998). The SSF interfacial force model was extended in the solver. The pore space was initially saturated with oil while brine was injected along the x-direction using a relaxed-fixed injection rate boundary condition designed to gradually increase the injection rate to the target rate (Fig. 2(b)). A fixed pressure condition was considered at the outlet boundary, and no-slip boundary condition was imposed at the fluid-solid interfaces. The detailed fluid properties are shown in Table 2.

### 3. Validation

Several studies have validated direct two-phase flow simulations against micro-scale experimental water flooding results, including pore scale fluid dynamics and distribution. Pore-by-pore comparison showed a good agreement between simulation and experiment (Nabizadeh et al., 2019; Alizadeh and Fatemi, 2021). Shams et al. (2021) also compared the results between multiphase flow simulation using high-resolution

synchrotron X-ray images of displacement in a limestone sample. Herein, the validity of the flow model was verified using microfluidics results. A pore-doublet geometry similar to the experiments was designed, and the tests were simulated using the numerical solver (Chatzis and Dullien, 1983). As illustrated in Fig. 3, the wetting phase is trapped in the narrower side channel during the drainage process, and no residual oil would be present with the hierarchical imbibition process from the smaller and then the larger channel. Similar behavior was predicted for both the drainage and imbibition processes. Consistent with previous studies, the displacement process has been found to be 100% efficient for all rates of injection of the wetting phase in the traditional pore doublets (Namaee-Ghasemi et al., 2021). Moreover, a pore-doublet model incorporating a large bulge (large pore) has also been investigated (Fig. 4). It was observed that oil was trapped in the pore space (point C) with large aspect ratio ( $D_3/D_2 = 2.47$ ). The main reasons for this kind of trapping are (i) that the interface at the point C remains stationary, while the wetting phase has already arrived in point B (Fig. 4(b)); (ii) the snap-off of the non-wetting phase at point B due to the existence of capillary instability conditions (Fig. 4(d)). The latter is also the main mechanism during the formation of residual oil ganglia in complex pore structures. However, the chances of entrapment by the above snap-off mechanism are substantially decreased if the capillary number is higher.

## 4. Results and discussion

In this section, the results of two-phase flow simulations performed on the complex porous media are presented. Pore-scale fluid occupancy maps were provided to explain the observed oil trapped trends. Firstly, a detailed analysis of the fluid displacement correlations with pore-throat geometry is given. Secondly, the residual oil mobilization during the continuous or discontinuous imbibition simulation is discussed.

### 4.1 Correlation of fluid displacement with pore-throat geometry

Assuming that the oil phase forms a connected network spanning over the porous model, water flooding was deployed

**Table 2.** Fluid properties used in the simulation.

Interfacial tension (mN/m)	Contact angle (°)	Oil		Brine	
		Density (kg/m <sup>3</sup> )	Viscosity (Pa·s)	Density (kg/m <sup>3</sup> )	Viscosity (Pa·s)
36	45	800	$9.6 \times 10^{-3}$	1,000	$6.4 \times 10^{-4}$

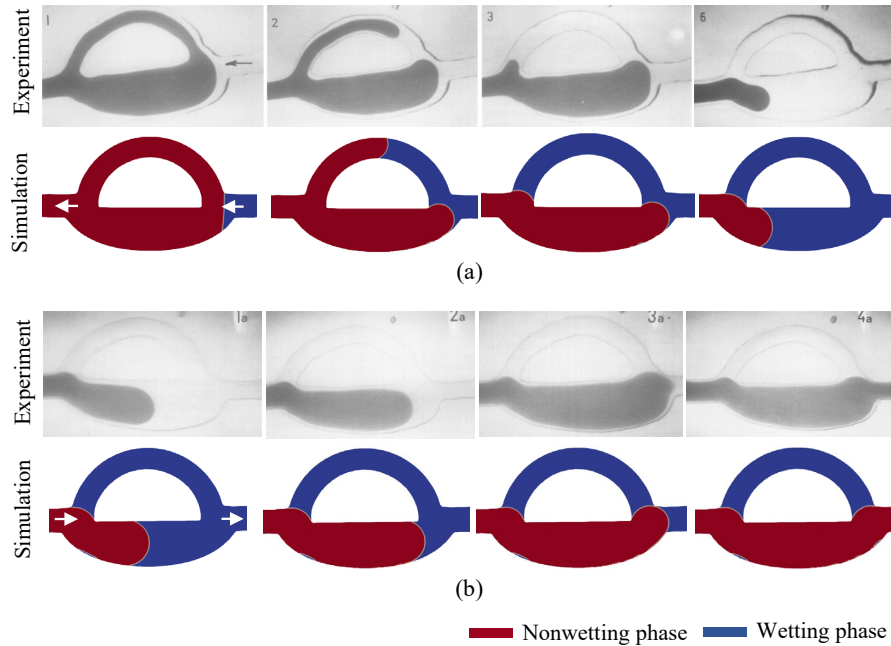


**Fig. 3.** Comparison of simulation results and experimental data. (a) Imbibition process (from left to right:  $t=0.0022$  s,  $0.011$  s,  $0.082$  s, and  $0.102$  s) and (b) drainage process (from left to right:  $t=0.016$  s,  $0.027$  s,  $0.032$  s, and  $0.046$  s).

at a low flow rate of  $130 \mu\text{m/s}$  to reduce the influence of viscous force. Affected by the non-homogeneity of pore structure, a water finger inside the porous space formed, in which water bypasses the oil phase in the larger pores (Fig. 5). As the water displacement continued, the first finger breakthroughs occurred after  $0.04$  pore volume (PV) was injected. Other collateral pathways also developed gradually alongside this main flow pathway in the late high water cut stage. The swept areas spread more widely. In the final stage of water flooding, the remaining oil saturation  $S_o$  dropped to  $0.49$ . The mechanism of trapping was mostly due to the bypassing and snap-off of the oil ganglia residing in large pores. However, the disconnection and trapping of residual oil might have been underestimated, while it is hard to simulate the dynamic of thin water film in a complex porous model due to the extreme instability of large interphase area between the liquids (Cai et al., 2022).

As brine is the wetting phase, it tends to enter the well-connected smaller throats and pores because of capillary force, and a significant amount of residual oil in the relatively large pores would be bypassed and trapped behind the water flooding front. The competition between flow paths influence the distribution of stagnant and flowing regions. On the other hand, the oil-brine interface behaviors determine the balance of forces and the equilibrium state of the oil cluster in the complex pore-scale network. The interface curvature of water/oil meniscus in the porous model depends on the specific

pore geometry and shape of the pore-throat connections. When pore filling events occur, the interfaces reach adjacent throats and further move toward the center of pores, eventually leading to piston-like oil displacement. Once these menisci join in a pore/throat and disconnect the original continuous oil phase, the oil ganglia would be pinned in their location. This process is known as snap-off, which results in reduced oil phase connectivity and delayed recovery. Aided by the pore-throat geometry (convergent-divergent) and the irregular shape of the pore space, the instability of the interface contributes significantly to the entrapment of residual oil.

The mean curvatures of oil clusters were measured on smoothed interphase surfaces during water flooding (Fig. 6). This was achieved by determining the average of the two principal curvatures, which were represented by the eigenvalues and eigenvectors of the quadratic form generated using the local oil-brine surface scalar field (Alhammadi et al., 2020). The average curvature is close to zero at a water saturation of  $0.11$ , which indicates an overall well-connected oil distribution. The curvature would decrease when the brine enters the pore body during the displacement process. As the water saturation increases, more and more disconnected oil clusters with higher curvature values become trapped, and the peaks of curvature distribution curve shift to the right. A similar phen-

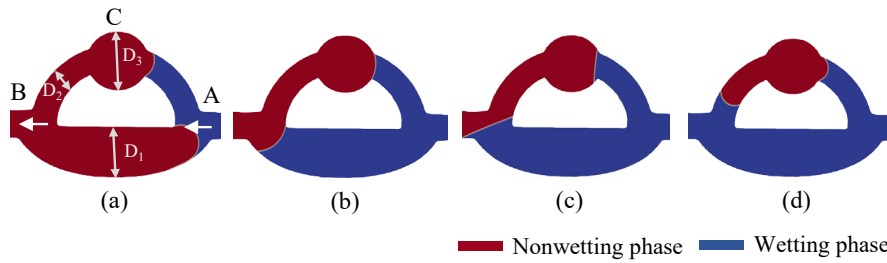


**Fig. 4.** Imbibition simulation in a pore-doublet model incorporate with large bulge. (a)  $t=0.027$  s, (b)  $t=0.11$  s, (c)  $t=0.12$  s and (d)  $t=0.16$  s. The flow direction is from point A to point B.

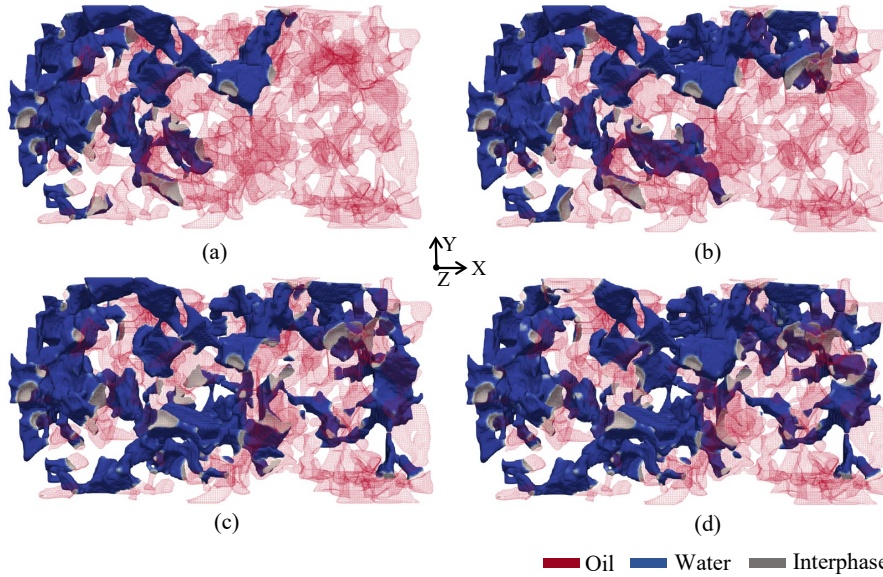


**Fig. 5.** Fluid distribution within the sandstone sample during imbibition. From (a) to (d), the oil saturation gradually decreases. (a) 0.03 PV,  $t = 0.31$  s,  $S_o = 0.78$ ; (b) 0.04 PV,  $t = 0.51$  s,  $S_o = 0.68$ ; (c) 0.40 PV,  $t = 4.60$  s,  $S_o = 0.56$  and (d) 0.85 PV,  $t = 8.35$  s,  $S_o = 0.49$ .

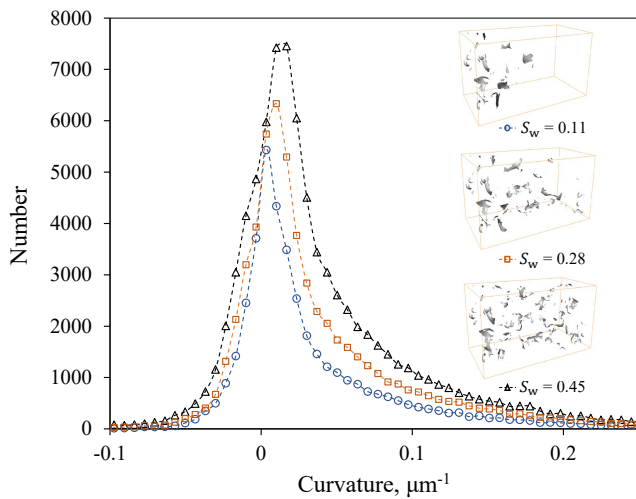


**Fig. 6.** Curvature distributions for the phase interfaces during imbibition.

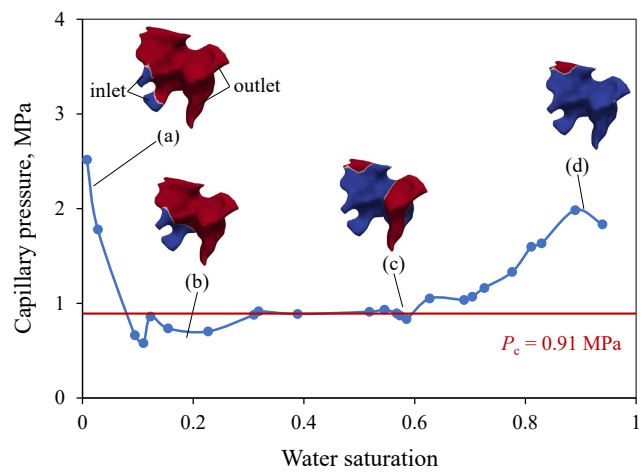


**Fig. 7.** Evolution of capillary pressure during  $I_2$  displacement as a function of pore geometry (blue: Water; red: Oil; grey: Phase interface). The red line represents the capillary pressure value calculated by the approximate expression. (a) Meniscus of the two-phase interphase in throat, (b) formation of  $I_2$  displacement, (c) oil cluster displaced by brine and (d) the residual oil formed in corner after displacement.

omenon has been observed in the experimental results with a water-wet Bentheimer sandstone (Lin et al., 2019). Meanwh-

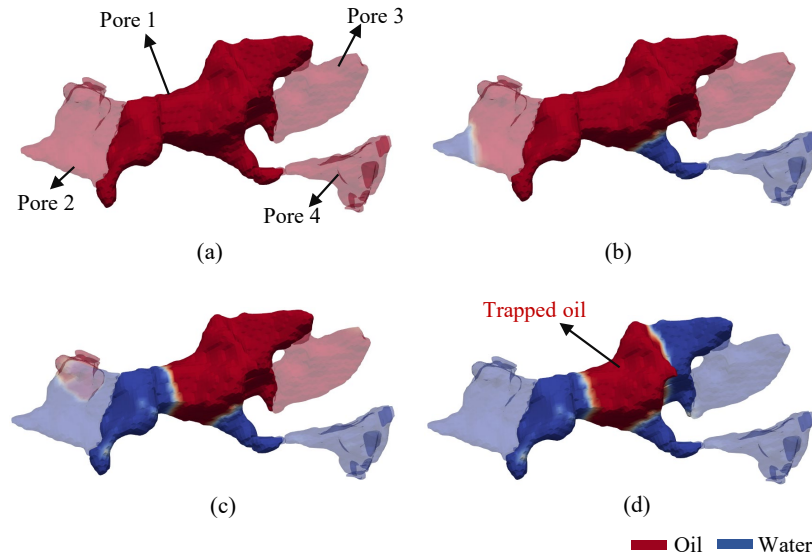


**Fig. 8.** Pore-filling and snap-off events during imbibition. The analysis was performed on a small subset of  $307 \times 488 \times 465 \mu\text{m}^3$ . (a)  $t = 0$  s, (b)  $t = 0.11$  s, (c)  $t = 0.27$  s and (d)  $t = 0.42$  s.

ile, the peak values are considered as corresponding to the capillary pressure at which the majority of snap-off occurred (Armstrong et al., 2012).

The fluid invasion process during imbibition occurs as a combination of piston-like displacements, cooperative pore-fillings (characterized by  $I_n$ , where “ $n$ ” represents the number of surrounding throats filled with oil) and snap-offs (Ellman et al., 2024). As piston-like displacements do not change the connectivity of the oil phase, this work focuses on pore-filling and snap-off. The invasion  $P_c$  value of the geometry-based cooperative pore-filling events should take the local pore structure and fluid topology into account. The approximate expression for  $I_n$  filling processes in the literature is as follows (Blunt, 1998):

$$P_c(I_n) = \frac{2\sigma \cos \theta}{r_p + xbr_p} \quad (11)$$

where  $r_p$  represents the pore radius;  $b$  represents the coefficient whose size is approximately the average aspect ratio, while  $x$  is a random number between 0 and 1. Fig. 7 presents the evolution of capillary pressure during  $I_2$  displacement in a pore element. The approximate  $P_c$  value calculated by Eq. (11) (red line) is highly consistent with the numerically determined  $P_c$  values when the interphase is across the pore body, which means that it is affected by pore radius and aspect ratio. The residual oil formed in the corner after displacement is caused by the complex pore space. The important features of snap-off are shown in Fig. 8. It can be seen that brine (wetting phase) would fill into the oil-saturated pores in an order of smallest-to-largest. As the interface stops moving ahead a pore with an unfavorable aspect ratio where the curvature increase and capillary pressure decrease, new interfaces will be established in other connected pores simultaneously, and only the interface in the narrowest capillary starts advancing. Finally, the remaining oil snaps off and is formed when the

advancing water-oil interface reaches the node upstream of the pore network. This disconnection effect in the heterogeneous model has been investigated in the experimental work of Wu et al. (2021), and the pore doublet models incorporating pores with varying radii also can explain the entrapment of the non-wetting phase (Fig. 4).

There are mainly two kinds of pores during the imbibition process. In the late stage of water flooding, two-phase flow occurs in the swept pores with oil saturation of  $< 1$ . Residual oil clusters form influenced by the irregular pore structure. Meanwhile, the unswept pores constantly fill with oil because of its poor connectivity. To investigate how the geometric characteristics explain the observed residual oil distribution, the correlations between pore-throat geometric parameters and two-phase flow behavior were calculated, as shown in Fig. 9. The Pearson correlation coefficient  $r$  was used to determine the connection between two variables. Pearson’s  $r$  has a range of values from -1 to 1, with values near -1 or 1 indicating high correlations between the oil saturation and the relevant geometric parameter, and with 0 indicating no association:

$$r = \frac{\sum (x - \bar{x})(y - \bar{y})}{\sqrt{\sum (x - \bar{x})^2 \sum (y - \bar{y})^2}} \quad (12)$$

where  $\bar{x}$  and  $\bar{y}$  represent the mean values of variables  $x$  and  $y$ , respectively;  $y$  represents the pore-throat parameters, which include the average aspect ratio (the ratio of pore radius to the mean of all bounding throat radius), normalized pore radius (to characterize the location of a pore radius in the overall pore size distribution curve), pore shape factor, average throat shape factor, and pore coordination number.

Two kinds of relationships were investigated to clarify the effect of pore structure parameters on pore scale sweep efficiency and displacement efficiency, respectively. Firstly,  $x$  was used as an indicator function, which shows whether it is an unswept pore (value = 0) or a swept pore (value

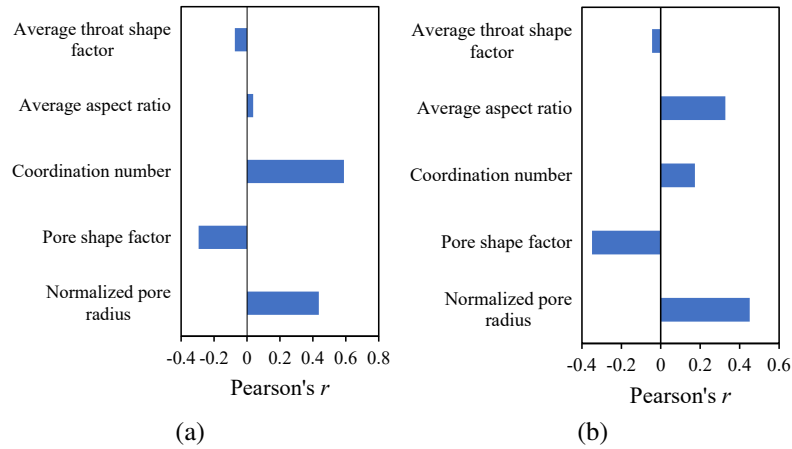


**Fig. 9.** Correlation with respect to pore type showing the relationship between residual oil distribution and pore structure. (a) Relationship between swept or unswept pores and pore-throat geometry and (b) relationship between residual oil distribution and pore-throat geometry.

**Table 3.** Structure parameters of three kinds of pores with different ranges of oil saturation in the breakthrough (Stage I) and last stages (Stage II).

Parameters	Swept pores				Unswept pores	
	$S_o = 0$		$S_o \in (0, 1)$		$S_o = 1$	
	Stage I	Stage II	Stage I	Stage II	Stage I	Stage II
Volume frequency (-)	0.063	0.069	0.562	0.804	0.375	0.127
Average pore radius ( $\mu\text{m}$ )	30.15	28.3	39.2	38.9	30.4	26.5
Average coordination number (-)	3	3.05	3.93	3.71	2.37	1.66
Average aspect ratio (-)	1.86	1.94	2.2	2.35	2.28	2.06

= 1). The analysis presented in Fig. 9(a) illustrates that the coordination number is strongly correlated to the flow path, which determines whether pores can be swept or not, with Pearson's  $r$  in the range 0.6. Pore radius and swept probability show a good correlation, indicating that water as a wetting phase tends to flow through smaller pores. The shape factor of pores and throats shows weak negative correlation. Because of the resistance force during the pore filling process, the pore shape factor could have a greater impact on the flow behavior of the wetting phase. Meanwhile, the average aspect ratio shows a weaker correlation, which means possibly no relationship. Next, changes in  $x$  were evaluated to describe the residual oil mobilization (residual oil saturation  $S_o = 0$  which means no trapped oil cluster, value = 0;  $S_o \in (0, 1)$  which means the presence of residual oil, value = 1) of all the swept pores. In addition to the pore radius, the average aspect ratio and pore shape factor also showed good correlation (Fig. 9(b)). Since aspect ratio is one of the important causes of snap-off, unfavorable aspect ratios usually lead to disconnection and stagnant oil cluster (Shams et al., 2021; Singh et al., 2022). Furthermore, the irregular pore shape would result in the formation of remaining oil in the corner. Similarly, the average throat shape factor has a weaker correlation with residual oil distribution. This unexpected result could be due to the limited

voxel count in throats (due to the low imaging resolution) which does not allow for the accurate estimation of shape factors (Raeini et al., 2017).

The average pore radius, average coordination number and average aspect ratio of the three kinds of pores in the breakthrough and last stages were also calculated (Table 3). Unswept pores have the lowest average coordination number, which lowers even more with the water flooding process, indicating that poor connectivity severely restricts the development of flow path. Pores with residual oil have a significantly larger pore-throat aspect ratio than those without, making oil ganglia more likely to break up and form residual oil. Moreover, the average radius of the pores with residual oil is larger than the pores without it. These pore sizes are in the upper range of the pore size distribution curves (Fig. 1). These observations are consistent with the findings reported in Fig. 9.

#### 4.2 Residual oil distribution during the continuous and discontinuous displacement modes

In order to further investigate the possibility of oil phase mobilization during the imbibition under different flow conditions, two displacement modes were considered: (i) The con-



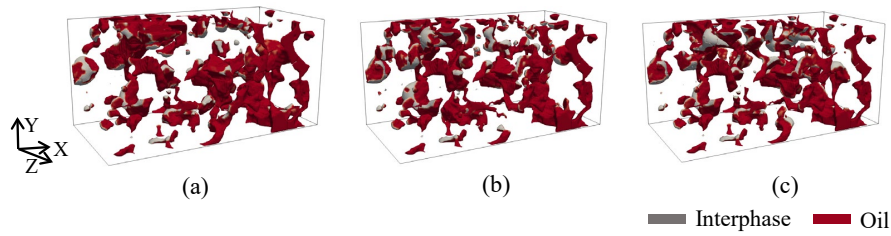


**Fig. 10.** Residual oil distribution map after water flooding for (a) Case 1, (b) Case 3, and (c) Case 5, respectively.

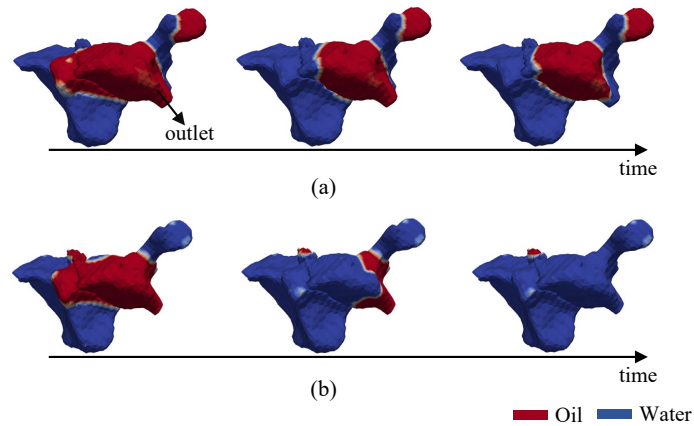


**Fig. 11.** Numerical simulation of the temporal evolution of snap-off and pore filling event for (a) Case 1 and (b) Case 3. The analysis was performed on a pore element with an aspect ratio of 2.02 ( $213 \times 201 \times 251 \mu\text{m}^3$ ).

**Table 4.** Flow parameters of each flow simulation.

Case	Flow rate ( $\mu\text{m/s}$ )	Capillary number (-)	Residual oil saturation (-)
1	130	$6.81 \times 10^{-6}$	0.495
2	650	$3.41 \times 10^{-5}$	0.472
3	1,300	$6.81 \times 10^{-5}$	0.443
4	650	$3.41 \times 10^{-5}$	0.491
5	1,300	$6.81 \times 10^{-5}$	0.448

tinuous displacement mode, which involved several water injection tests with increasing capillary numbers and same initial condition, and (ii) the discontinuous displacement mode, which included a multi-rate imbibition test. The simulation cases are shown in Table 4. The capillary number  $N_{ca} = (\mu_w u / \Phi \sigma \cos \theta) (\mu_w / \mu_o)^{0.4}$  is defined as the ratio of viscous forces to surface tension forces. The ratio of viscosity of brine  $\mu_w$  to viscosity of oil  $\mu_o$  was incorporated into this equation (Mohamed et al., 2020). It is imperative to mention that the micro-scale  $N_{ca}$  equation is dependent on the length scale, which means that the topology of oil clusters has been overlooked. Three simulation cases were set up for different capillary numbers with initial connected oil network (Case 1, Case 2, Case 3), and two cases (Case 4, Case 5) were simulated based on the residual oil distribution of Case 1. Due to the preceding imbibition simulation, the oil clusters were disconnected and trapped at this point.

For a specific pore space topology and wettability condition, the higher capillary number imbibition test produced similar distributions of trapped oil clusters with Case 1. Because of the pore-scale heterogeneity, an early breakthrough of brine was observed, causing a large amount of oil to be bypassed. As discussed earlier, the residual oil cluster tends to be trapped in the large pores with poor connectivity (Table 5). However, the simulation results showed that, under a given initial fluid configuration, the oil recovery was more efficient with an increase in capillary number (compare Case 1, Case 2 and Case 3). An additional recovery of 2.3% and 5.2% for Case 2 and Case 3, respectively, was observed. Considering the significantly higher brine flow rate, the brine phase can invade into some large and intermediate-sized pores to displace oil (Fig. 10). These findings are supported by the remaining oil distribution analysis based on the pore structure parameters (Table 5). Compared to Case 1, unswept pores were significantly reduced, and the average pore radius with residual oil slightly decreased at both the breakthrough and the final stage. Snap-off events could be suppressed, which means that more oil can be displaced through piston-like processes. This was associated with the fact that the average aspect ratio of pores without residual oil was higher than that in Case 1. As shown in Fig. 11, at a capillary number of  $6.81 \times 10^{-6}$ , the residual oil cluster snapped because of the swelling of water film in the pore-throat with an aspect ratio of 2.02 (Fig. 11(a)). Theoretically, the threshold of snap-off that results in the trapping of the non-wetting phase is encouraged by an aspect ratio greater than 2. However, as the viscous force

**Table 5.** Pore structure parameters of three kinds of pores with different ranges of oil saturation during the breakthrough (Stage I) and last stages (Stage II) in Case 3.

Parameters	Swept pores				Unswept pores	
	$S_o = 0$		$S_o \in (0, 1)$		$S_o = 1$	
	Stage I	Stage II	Stage I	Stage II	Stage I	Stage II
Volume frequency (-)	0.038	0.065	0.699	0.860	0.262	0.075
Average pore radius ( $\mu\text{m}$ )	29.6	28.4	38.86	37.08	28.75	25.91
Average coordination number (-)	2.6	2.68	3.91	3.53	2.15	1.54
Average aspect ratio (-)	1.69	2.2	2.32	2.31	2.16	1.82

**Table 6.** Pore structure parameters of three kinds of pores with different ranges of oil saturation before and after imbibition simulation in Case 5.

Parameters	Swept pores				Unswept pores	
	$S_o = 0$		$S_o \in (0, 1)$		$S_o = 1$	
	Before	After	Before	After	Before	After
Volume frequency (-)	0.069	0.051	0.804	0.875	0.127	0.074
Average pore radius ( $\mu\text{m}$ )	28.3	27.33	38.9	36.76	26.5	26.98
Average coordination number (-)	3.05	3.06	3.71	3.39	1.66	1.61
Average aspect ratio (-)	1.94	1.87	2.35	2.30	2.06	2.11

increases, the oil phase tends to keep connected, leading to piston-like displacement (Fig. 11(b)).

The residual oil saturation showed greater reduction under the continuous mode, during which the oil phase was connected prior to each imbibition (compare Case 2 and Case 4, Case 3 and Case 5). A reason for this is that most of the incremental recovery was attributed to the remobilization of previously trapped oil ganglia in the discontinuous imbibition simulation. Disconnected oil bubbles occupy a greater number of large pores, blocked by water phase, leading to a greater resistance to flow (Liu et al., 2021). These findings are supported by the residual oil saturation of Case 2 and Case 4, demonstrating that the pressure required to displace the connected oil clusters was notably lower than that needed to remobilize the trapped bubbles. However, they could still be remobilized when the capillary number exceeded a threshold value (Case 5). The saturation of trapped non-wetting phase was significantly reduced (4.7%). Similar to the continuous imbibition mode, conducting water flooding at a higher injection rate displaced oil from some larger well-connected pores (Fig. 10). The swept area further expanded and the final unswept pore volume ratio decreased to 0.074 (Table 6). The average coordination number of unswept pores also dropped. However, the oil phase enters some pores initially saturated with brine after the first time water flooding, so that the sweep efficiency for a single pore will decrease rather than improve (Li et al., 2017). As illustrated in Table 6, the volume ratio of pores without residual oil decreased in the final stage. Based on calculating the variation of remaining oil volume in the pore, about 20% pores will contain more oil after imbibition; more than half of these pores were consistent

with the continuous mode. The pores where oil bobbles were displaced usually had a larger pore radius (44.27  $\mu\text{m}$ ) and coordination number (4.5).

Furthermore, the oil bubbles would be slightly mobilized and redistributed before the residual oil saturation started to decrease. These kind of pore-scale displacement events occurred before the threshold of mobilization was reached during discontinuous displacement mode (Mohamed et al., 2020). The fragmentation and reconnection of trapped oil clusters prior to entrainment were observed (Fig. 12). The wetting phase can mobilize a confined oil bubble once it reaches a specific threshold value, which is dependent on the fluid properties, the diameter of the pore throats, and the size of the oil cluster (Liang et al., 2015). After increasing the injection velocity, the driven pressure is sufficient to overcome the Jamin effect and move the interfaces in the entry pore. Due to the higher drag force required, the narrower throat of the two constricted regions still block the oil bubble (Fig. 12(d)).

According to the fluid displacement correlations with the pore-throat geometry obtained above, a mobility coefficient was used to evaluate the displacement potential of remaining oil. The higher the mobility coefficient  $P_M$ , the greater the production potential:

$$P_M = \bar{P}_r \times \bar{C}_c \quad (13)$$

where  $\bar{C}_c$  represents the dimensionless connectivity coefficient, which characterizes the influence of coordination number on residual oil distribution.  $\bar{P}_r$  represents the dimensionless ratio of the threshold pressure for snap-off (Blunt, 2017), which characterizes the influence of the pore radius, average aspect ratio and pore shape factor on the disconnection effect (e.g.,

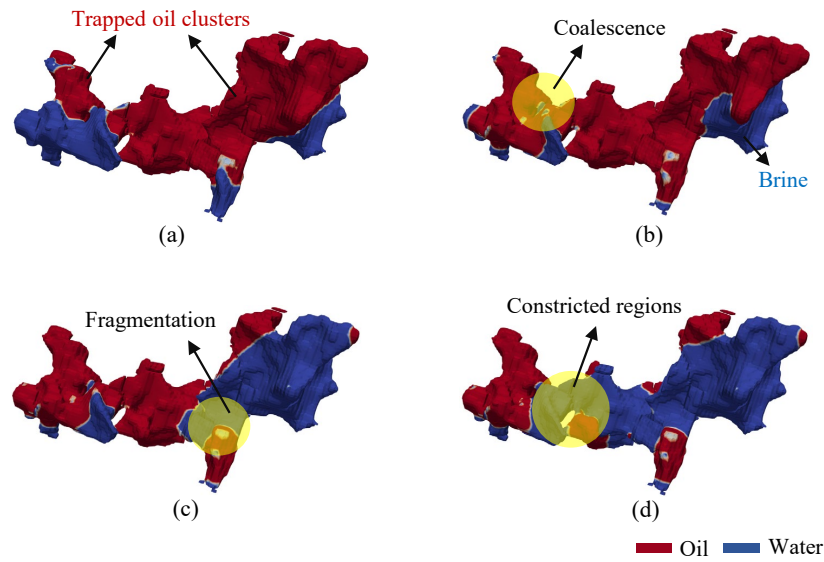


**Fig. 12.** (a) The initial oil distribution of Case 5,  $t = 0$  s, (b) reconnection,  $t = 0.0082$  s, (c) fragmentation of trapped oil during the discontinuous imbibition simulation,  $t = 0.020$  s and (d) the residual oil distribution after secondary water flooding,  $t = 0.025$  s.

snap-off) in each pore element. For a pore  $i$ :

$$P_{r,i} = \frac{r_{p,i}}{A_i r_{t,i}} \quad (14)$$

where  $r_{p,i}$  represents the pore radius;  $r_{t,i}$  represents the average throat radius of the pore  $i$ ;  $A_i$  represents a coefficient dependent on the pore geometry, with a range from 2 for a circular pore to 1 for more slit-like shapes.  $A_i = (1 + S_i)$  is used here, where  $S_i$  represents the pore shape factor.

The above relations were used to quantify the effect of pore geometry and displacement mode during the imbibition process. As presented in Fig. 13(a), there are no unswept pores with  $P_M$  greater than 0.5 (region A). Furthermore, oil clusters trapped in pores with  $P_M$  less than 0.1 were hard to displace in all the simulation cases (region C). The average recovery degree of region A, region B and region C in different simulation cases are as shown in Fig. 13(b). The results also confirm that the mobilization of residual oil trapped in pores with higher  $P_M$  is controlled by the capillary number. The recovery degree in these pores was improved, whereas the average recovery degree of region A for Case 3 and Case 5 was significantly reduced. Although the discontinuous displacement Case 5 have the same capillary number with Case 3, the enhancement effect diminished due to the greater resistance of disconnected oil clusters. The average recovery degree of region C for Case 3 slightly improved, which means that oil in pores with low  $P_M$  was mobilized. In contrast, it barely changed under the discontinuous mode (Case 5). The average recovery degree of region B for Case 5 even reduced, which might be caused by the rearrangement of oil clusters. Unfortunately, the number of points (characterizing the pore elements in our model) was limited by computing power. More simulation data based on different types of porous models need to be analyzed in future work.

## 5. Conclusions

In this study, the pore-scale physics of two-phase flow under the high water cut stage were investigated in a water-wet heterogeneous porous media. Brine injections with different capillary number were performed in a sandstone model under continuous and discontinuous displacement conditions. By extracting a labeled mesh of pore space characterized by different pore elements and superimposing it on the simulation model, the pore structure characteristics favorable for residual oil were analyzed. Several new attributes of the oil distribution mechanism were identified from the two-phase flow simulations. The main findings can be summarized as follows:

- 1) The pore-throat geometry and the irregular shape of the pore space in heterogeneous porous media have a great impact on two-phase flow behavior. The trapping mechanism is mostly due to the bypassing and snap-off of the oil ganglia residing in large pores.
- 2) The relationship between residual oil distribution and pore structure parameters was quantitatively characterized. The coordination number is strongly correlated to the flow path, and the pore radius, average aspect ratio and pore shape factor show good correlation with the formation of residual oil clusters.
- 3) The statistical analysis of trapped oil revealed that the brine phase can invade into some large and intermediate-sized pores to displace oil under higher brine flow rate. The snap-off events can be suppressed, which means that more piston-like pore events happen. The above two factors are responsible for the decline in remaining oil saturation during water injections with increasing capillary number.
- 4) By incorporating the correlations of displacement events with pore-throat geometry, the displacement modes with

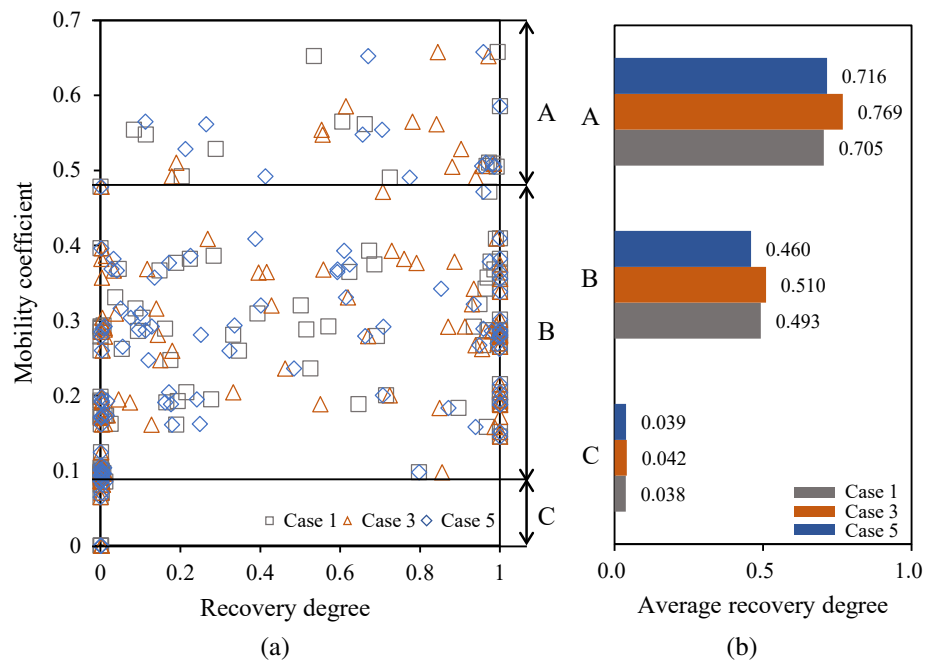


**Fig. 13.** (a) Mobility coefficient PM versus recovery degree across each pore element in test cases. Three regions A, B and C were divided based on the point distribution and (b) the average recovery degree of region A, region B and region C in different cases.

different capillary number were evaluated. Because of the flow resistance of disconnected oil bubbles, the residual oil saturation reduces to a greater extent under the continuous mode during which the oil phase is connected prior to each imbibition. The residual oil trapped in larger well-connected pores tend to be displaced for production.

In summary, direct pore-scale imbibition simulations were conducted to investigate the correlations of residual oil distribution with the pore structure parameters, which could be helpful to further improve the existing predictive models of residual oil, especially for sandstone reservoirs that have already entered the high water cut development stage. Pore space models with a reasonable distribution of contact angles will be performed to present more realistic results. Future work will focus on the effect of spatially heterogeneous wettability on the formation and mobilization mechanisms of residual oil in 3D porous media, validated against experimental data in cores.

## Acknowledgements

We would like to express our gratitude to for the financial support of the following organizations: The National Natural Science Foundation of China (Nos. U23A20595, 52034010 and 52288101), the National Key Research and Development Program of China (No. 2022YFE0203400), the Qingdao Natural Science Foundation (No. 23-2-1-230-zyyd-jch), the Fundamental Research Funds for the Central Universities (No. 23CX10004A), and the Program for Changjiang Scholars and Innovative Research Team in University (No. IRT\_16R69).

## Addition information: Author's email

lisitsavv@ipgg.sbras.ru (V. Lisitsa).

## Conflict of interest

The authors declare no competing interest.

**Open Access** This article is distributed under the terms and conditions of the Creative Commons Attribution (CC BY-NC-ND) license, which permits unrestricted use, distribution, and reproduction in any medium, provided the original work is properly cited.

## References

- Alhammadi, A. M., Gao, Y., Akai, T., et al. Pore-scale X-ray imaging with measurement of relative permeability, capillary pressure and oil recovery in a mixed-wet microporous carbonate reservoir rock. *Fuel*, 2020, 268: 117018.
- Alizadeh, M., Fatemi, M. Pore-doublet computational fluid dynamic simulation of the effects of dynamic contact angle and interfacial tension alterations on the displacement mechanisms of oil by low salinity water. *International Journal of Multiphase Flow*, 2021, 143: 103771.
- Andersson, L., Herring, A., Schlüter, S., et al. Defining a novel pore-body to pore-throat "Morphological Aspect Ratio" that scales with residual non-wetting phase capillary trapping in porous media. *Advances in Water Resources*, 2018, 122: 251-262.
- Andrew, M., Bijeljic, B., Blunt, M. J. Pore-scale contact angle measurements at reservoir conditions using X-ray microtomography. *Advances in Water Resources*, 2014, 68: 24-31.
- Armstrong, R. T., Porter, M. L., Wildenschild, D. Linking

- pore-scale interfacial curvature to column-scale capillary pressure. *Advances in Water Resources*, 2012, 46: 55-62.
- Aziz, R., Niasar, V., Erfani, H., et al. Impact of pore morphology on two-phase flow dynamics under wettability alteration. *Fuel*, 2020, 268: 117315.
- Blunt, M. J. Physically-based network modeling of multiphase flow in intermediate-wet porous media. *Journal of Petroleum Science and Engineering*, 1998, 20(3): 117-125.
- Blunt, M. J. *Multiphase Flow in Permeable Media: A Pore-Scale Perspective*. London, UK, Cambridge University Press, 2017.
- Blunt, M. J., Bijeljic, B., Dong, H., et al. Pore-scale imaging and modelling. *Advances in Water Resources*, 2013, 51: 197-216.
- Brackbill, J. U., Kothe, D. B., Zemach, C. A continuum method for modeling surface tension. *Journal of Computational Physics*, 1992, 100(2): 335-354.
- Bultreys, T., Singh, K., Raeini, A. Q., et al. Verifying pore network models of imbibition in rocks using time-resolved synchrotron imaging. *Water Resources Research*, 2020, 56(6): e2019WR026587.
- Cai, J., Chen, Y., Liu, Y., et al. Capillary imbibition and flow of wetting liquid in irregular capillaries: A 100-year review. *Advances in Colloid and Interface Science*, 2022, 304: 102654.
- Chatzis, I., Dullien, F. A. L. Dynamic immiscible displacement mechanisms in pore doublets: Theory versus experiment. *Journal of Colloid and Interface Science*, 1983, 91(1): 199-222.
- Ellman, S., Mascini, A., Bultreys, T. Validating mechanistic models of fluid displacement during imbibition. *Advances in Water Resources*, 2024, 183: 104590.
- Gao, Y., Raeini, A. Q., Blunt, M. J., et al. Dynamic fluid configurations in steady-state two-phase flow in Bentheimer sandstone. *Physical Review E*, 2021, 103(1): 013110.
- Gong, W., Liu, Y., Xi, C., et al. Dynamic characterization of residual oil during long-term waterflooding experiments in heterogeneous porous structures. *Fuel*, 2024, 356: 129567.
- Graveleau, M., Soulaire, C., Tchepeli, H. A. Pore-scale simulation of interphase multicomponent mass transfer for subsurface flow. *Transport in Porous Media*, 2017, 120(2): 287-308.
- Guo, Y., Zhang, L., Zhu, G., et al. A Pore-scale investigation of residual oil distributions and enhanced oil recovery methods. *Energies*, 2019, 12(19): 3732.
- Joekar-Niasar, V., Hassanzadeh, S. M., Dahle, H. K. Non-equilibrium effects in capillarity and interfacial area in two-phase flow: Dynamic pore-network modelling. *Journal of Fluid Mechanics*, 2010, 655: 38-71.
- Kimbrel, E. J. H., Wildenschild, D., Herring, A. L., et al. The effect of original and initial saturation on residual non-wetting phase capillary trapping efficiency. *International Journal of Greenhouse Gas Control*, 2022, 120: 103758.
- Li, J., Jiang, H., Wang, C., et al. Pore-scale investigation of microscopic remaining oil variation characteristics in water-wet sandstone using CT scanning. *Journal of Natural Gas Science and Engineering*, 2017, 48: 36-45.
- Li, J., Liu, Y., Gao, Y., et al. Effects of microscopic pore structure heterogeneity on the distribution and morphology of remaining oil. *Petroleum Exploration and Development*, 2018, 45(6): 1112-1122.
- Liang, M., Yang, S., Miao, T., et al. Minimum applied pressure for a drop through an abruptly constricted capillary. *Microfluidics and Nanofluidics*, 2015, 19(1): 1-8.
- Lin, Q., Bijeljic, B., Berg, S., et al. Minimal surfaces in porous media: Pore-scale imaging of multiphase flow in an altered-wettability Bentheimer sandstone. *Physical Review E*, 2019, 99(6): 063105.
- Liu, S., Dou, X., Zeng, Q., et al. Critical parameters of the Jamin effect in a capillary tube with a contracted cross section. *Journal of Petroleum Science and Engineering*, 2021, 196: 107635.
- Mascini, A., Boone, M., Van Offenwert, S., et al. Fluid invasion dynamics in porous media with complex wettability and connectivity. *Geophysical Research Letters*, 2021, 48(22): e2021GL095185.
- Michels, R., Siebert, D. N., dos Santos, L. O. E. Investigation on the influence of capillary number on drainage in porous media using a lattice Boltzmann method. *Journal of Petroleum Science and Engineering*, 2021, 205: 108918.
- Mohamed, A. I. A., Khishvand, M., Piri, M. A pore-scale experimental investigation of process-dependent capillary desaturation. *Advances in Water Resources*, 2020, 144: 103702.
- Nabizadeh, A., Adibifard, M., Hassanzadeh, H., et al. Computational fluid dynamics to analyze the effects of initial wetting film and triple contact line on the efficiency of immiscible two-phase flow in a pore doublet model. *Journal of Molecular Liquids*, 2019, 273: 248-258.
- Namaee-Ghasemi, A., Ayatollahi, S., Mahani, H. Pore-scale simulation of the interplay between wettability, capillary number and salt dispersion on the efficiency of oil mobilization by low salinity waterflooding. *SPE Journal*, 2021, 26(6): 4000-4021.
- Nguyen, V. H., Sheppard, A. P., Knackstedt, M. A., et al. The effect of displacement rate on imbibition relative permeability and residual saturation. *Journal of Petroleum Science and Engineering*, 2006, 52(1): 54-70.
- Pak, T., Butler, I. B., Geiger, S., et al. Droplet fragmentation: 3D imaging of a previously unidentified pore-scale process during multiphase flow in porous media. *Proceedings of the National Academy of Sciences*, 2015, 112(7): 1947-1952.
- Pak, T., Rabbani, H. S., Qaseminejad Raeini, A., et al. Effects of the pore morphology on multiphase fluid displacement in porous media-A high-resolution modeling investigation. *ACS Omega*, 2023, 8(4): 3889-3895.
- Patel, H. V., Kuipers, J. A. M., Peters, E. A. J. F. Effect of flow and fluid properties on the mobility of multiphase flows through porous media. *Chemical Engineering Science*, 2019, 193: 243-254.
- Pereira, G. G. Fluid flow, relative permeabilities and capillary pressure curves through heterogeneous porous media.

- Applied Mathematical Modelling, 2019, 75: 481-493.
- Qin, X., Xia, Y., Qiao, J., et al. Modeling of multiphase flow in low permeability porous media: Effect of wettability and pore structure properties. *Journal of Rock Mechanics and Geotechnical Engineering*, 2023, in press, <https://doi.org/10.1016/j.jrmge.2023.06.007>.
- Raeini, A. Q., Bijeljic, B., Blunt, M. J. Generalized network modeling: Network extraction as a coarse-scale discretization of the void space of porous media. *Physical Review E*, 2017, 96(1): 013312.
- Raeini, A. Q., Blunt, M. J., Bijeljic, B. Modelling two-phase flow in porous media at the pore scale using the volume-of-fluid method. *Journal of Computational Physics*, 2012, 231(17): 5653-5668.
- Rusche, H. *Computational Fluid Dynamics of Dispersed Two-Phase Flows at High Phase Fractions*. London, UK, Imperial College, 2002.
- Shams, M., Raeini, A. Q., Blunt, M. J., et al. A study to investigate viscous coupling effects on the hydraulic conductance of fluid layers in two-phase flow at the pore level. *Journal of Colloid and Interface Science*, 2018, 522: 299-310.
- Shams, M., Singh, K., Bijeljic, B., et al. Direct numerical simulation of pore-scale trapping events during capillary-dominated two-phase flow in porous media. *Transport in Porous Media*, 2021, 138: 443-458.
- Singh, K., Bultreys, T., Raeini, A. Q., et al. New type of pore-snap-off and displacement correlations in imbibition. *Journal of Colloid and Interface Science*, 2022, 609: 384-392.
- Singh, K., Menke, H., Andrew, M., et al. Dynamics of snap-off and pore-filling events during two-phase fluid flow in permeable media. *Scientific Reports*, 2017, 7(1): 5192.
- Ubbink, O., Issa, R. I. A method for capturing sharp fluid interfaces on arbitrary meshes. *Journal of Computational Physics*, 1999, 153(1): 26-50.
- Wang, S., Chen, L., Feng, Q., et al. Pore-scale simulation of gas displacement after water flooding using three-phase lattice Boltzmann method. *Capillarity*, 2023a, 6(2): 19-30.
- Wang, W., Xie, Q., An, S., et al. Pore-scale simulation of multiphase flow and reactive transport processes involved in geologic carbon sequestration. *Earth-Science Reviews*, 2023b, 247: 104602.
- Wang, W., Xie, Q., Wang, H., et al. Pseudopotential-based multiple-relaxation-time lattice Boltzmann model for multicomponent and multiphase slip flow. *Advances in Geo-Energy Research*, 2023c, 9(2): 106-116.
- Wang, X., Yin, H., Zhao, X., et al. Microscopic remaining oil distribution and quantitative analysis of polymer flooding based on CT scanning. *Advances in Geo-Energy Research*, 2019, 3(4): 448-456.
- Weller, H. G., Tabor, G., Jasak, H., et al. A tensorial approach to computational continuum mechanics using object-oriented techniques. *Computer in Physics*, 1998, 12(6): 620-631.
- Wu, D. S., Hu, R., Lan, T., et al. Role of pore-scale disorder in fluid displacement: Experiments and theoretical model. *Water Resources Research*, 2021, 57(1): e2020WR028004.
- Yang, P., Guo, H., Yang, D. Determination of residual oil distribution during waterflooding in tight oil formations with NMR relaxometry measurements. *Energy & Fuels*, 2013, 27(10): 5750-5756.
- Yang, Y., Cai, S., Yao, J., et al. Pore-scale simulation of remaining oil distribution in 3D porous media affected by wettability and capillarity based on volume of fluid method. *International Journal of Multiphase Flow*, 2021, 143: 103746.
- Yang, Y., Tao, L., Iglauer, S., et al. Quantitative statistical evaluation of micro residual oil after polymer flooding based on X-ray micro computed-tomography scanning. *Energy & Fuels*, 2020, 34(9): 10762-10772.
- Yang, Y., Wang, J., Wang, J., et al. Pore-scale modeling of coupled CO<sub>2</sub> flow and dissolution in 3D porous media for geological carbon storage. *Water Resources Research*, 2023, 59(10): e2023WR035402.
- Yang, Y., Yang, H., Tao, L., et al. Microscopic determination of remaining oil distribution in sandstones with different permeability scales using computed tomography scanning. *Journal of Energy Resources Technology*, 2019, 141(9): 092903.
- Zacharoudiou, I., Chapman, E. M., Boek, E. S., et al. Pore-filling events in single junction micro-models with corresponding lattice Boltzmann simulations. *Journal of Fluid Mechanics*, 2017, 824: 550-573.
- Zhang, C., Zhang, Q., Wang, W., et al. Capillary and viscous forces during CO<sub>2</sub> flooding in tight reservoirs. *Capillarity*, 2022, 5(6): 105-114.
- Zhang, Y., Lin, C., Ren, L. Flow patterns and pore structure effects on residual oil during water and CO<sub>2</sub> flooding: In situ CT scanning. *Energy & Fuels*, 2023, 37(20): 15570-15586.